Supporting Information for "The Earth's surface controls the depth-dependent seismic radiation of megathrust earthquakes"

Jiuxun Yin[1], Marine A. Denolle[1,2]

[1]Department of Earth and Planetary Sciences, Harvard University

[2]Department of Earth and Space Sciences, University of Washington

Contents of this file

1. Text S1 to S2
2. Figures S1 to S13
3. Table S1

Additional Supporting Information (Files uploaded separately) Caption of the figures. Each figure contains 8 subfigures to show model settings and results. (a) The structure of model: topography, fault geometry, P wave velocity. The blue outlined region (if any) indicates the region where we set the V_P/V_S ratio to the given value. (b) Initial stress distributions along depth (black line: initial shear stress τ_0; gray line: initial effective normal stress $\bar{\sigma}_0$. (c) Parameters of used friction law along depth: upper X-axis shows the friction coefficients (red dashed line: dynamic friction coefficient μ_d; red solid line: static friction coefficient μ_s), bottom X-axis shows the critical slip D_c in black line. (d) Space-time evolution of the rupture (in blue colormap) and of selected points on the fault (black lines), including the one at the trench/surface (thick black line). Gray and red lines show the updip- and downdip-propagating rupture front, respectively. We estimate the rupture velocity by linear fitting the location and time of rupture front. Light purple lines (if any) indicate the super-shear rupture front triggered by free surface and shallow compliant structures. (e) Slip-rate functions at each fault segment, aligned to their onset time (when rupture front arrives). The location of the fault segment center taken as the alongdip distance from the trench is indicated by the gray colormap. (f) Normalized Fourier amplitude spectra corresponding to the slip-rate functions shown in (e). The same color scheme is used to indicate the fault segment location. (g) moment-rate density function averaged along the entire fault. (h) The along-dip best-fit spectral parameters of the spectra in (f) as well as its 95% confidence interval. The right Y-axis shows the corner frequency f_c in red. The left Y-axis shows the spectral falloff rate n in blue.

Introduction

Text S1 presents the information about the back-projection observations (Figure 1 in the main text). Text S2 presents detailed information about dynamic rupture modeling. The model setup details include model setting, friction, initial stress, and software information. All simulation settings and results of each model are included in Supporting Information 2, which is a Zip file of Figures including the model parameters ((a) structures, (b) stress, (c) friction), simulations results ((d) - (g)) and the fitting of spectral parameters ((h) corner frequency f_c and spectral falloff rate n).

1. Text S1. back-projection analysis

1.1. Recent large earthquake BP images

We show the back-projection (BP) results of the Mw 9.0 2011 Tohoku-oki earthquake, the Mw 7.9 2015 Gorkha earthquake, and the Mw 8.3 2015 Illapel earthquake. We obtain these BP results using a high-resolution improved Compressive Sensing back-projection (imCS-BP) method that we developed. Detailed information about this methodology can be found in Yin, Denolle, and Yao (2018).

We download the available teleseismic P wave velocity seismograms of the 2011 Tohoku earthquake recorded by the USArray stations (TA array, Fig. S1a - b) in North America (TA `doi:10.7914/SN/TA`, data is downloaded using Wilber 3 of the Incorporated Research Institutions for Seismology Data Management Center, IRIS-DMC, `http://ds.iris.edu/wilber3/find_event`). The raw data is first processed by removing the mean, trend, and instrumental responses. Then we filter the waveforms (Butterworth filter, order 2) into the low-frequency (LF) band (0.05 - 0.5 Hz) and high-frequency (HF) band (0.5 - 1 Hz) and align the waveforms based on the P wave arrival time Fig. S1a - b. The sliding time window technique is used to get the time evolution of the earthquake rupture, and we choose a window length of 14 s for the 0.05 – 0.5 Hz LF band and 8 s for the 0.5 – 1 Hz HF band. The step of the moving time window is set 2 s. Within each time window, we apply the imCS-BP with auto-adaptive source grid refinement (Yin et al., 2018) to locate the coherent peaks and finally get the back-projection images of the Tohoku earthquakes in different frequency bands (Fig. S1c - d). In the main text, we integrate the BP results over the entire duration to construct a total BP image for each frequency band (Fig. 1a). Our BP results of the 2011 Tohoku earthquake are well consistent with the relevant previous studies (Wang & Mori, 2011; Yao et al., 2011; Lay et al., 2012).

For the 2015 Nepal and Chile earthquakes, we use the same imCS-BP technique and the same USArray data as our previous studies (Yin et al., 2017, 2018). The waveforms of the Mw 7.9 2015 Gorkha earthquake are filtered at 0.05 - 0.25 Hz and 0.25 - 1.0 Hz frequency bands while the waveforms of the Mw 8.3 2015 Illapel earthquake are filtered at 0.05 - 0.5 Hz and 0.5 - 1.0 Hz frequency bands. The difference in the frequency band is due to handling different magnitudes of earthquakes (Yin & Denolle, 2019). Here we simply show the data and BP results of both events (Figs. S2 - S3) and refer to the previous publications for more details on the interpretation and reliability of the images given the source and receiver array configuration (Yin et al., 2016, 2017, 2018).

1.2. Analysis of the IRIS BP database

We further explore whether the depth-frequency relation exists for most megathrust earthquakes with the help of the back-projection database of the Incorporated Research Institutions for Seismology (IRIS). The IRIS back-projection database (Incorporated Research Institutions for Seismology Data Management Center, 2011) automatically generates the BP images from three regional arrays (NA: northern America; EU: Europe; AU: Australia) and the Global Seismic Network (GSN) for all the M6.5+ earthquakes since 1995 (Incorporated Research Institutions for Seismology Data Management Center, 2011).

The three regional arrays can produce the HF (0.25 - 1.00 Hz) BP images, and the GSN can produce the LF (0.05 - 0.25 Hz) BP images. This provides an opportunity to compare the depth-frequency relation systematically (i.e., with a single method) instead of making an inventory of results based on different methods applied to different earthquakes.

We collect the HF and LF BP peaks of all the 842 earthquakes present in the IRIS database (available at `http://ds.iris.edu/spud/back-projection`, last accessed on 02/27/2021). Among the events from the IRIS database, we only select those with BP results from all four arrays/networks. Because the BP results are recovered from the teleseismic P waves, which have poor depth resolution, we project the latitude and longitude of the BP peaks onto the corresponding Slab2 slab model (Hayes et al., 2018) to infer the depth of the BP results. Only 461 earthquakes (mostly megathrust earthquakes) within the latitude-longitude range of the available Slab2 models are kept.

Next, we calculate the average depth of all the BP peaks weighted by the BP peak amplitude for each array. We define the average depth as the BP centroid depth of the earthquake for each specific array. In this way, we can obtain the BP centroid depth from the GSN BP results in the low-frequency band of 0.05 - 0.25 Hz and the 3 estimates of the HF BP centroid depths from the dense regional arrays NA, AU, and EU in the high-frequency band of 0.25 - 1 Hz. Because we focus on the megathrust earthquakes in this study, we only keep the 245 events with BP centroid depth less than 70 km and the comparison results of all three regional arrays are shown in Fig. S4.

Finally, we take the mean the HF BP centroid depths across all three arrays as the representative HF BP centroid depth and show the comparison with LF BP centroid from GSN in Fig. 1d of the main text. We also show the same results for the deep earthquakes with depth from 70 km to 700 km in Fig. S5 to show that the frequency-depth relation disappears for deep earthquakes.

2. Text S2. Details on the dynamic rupture simulations

2.1. Model setting

The simulation domain is a semicircle domain with a radius of 350 km and centered at X = 150 km, Y = 0 km, and a traction-free surface. The simulation domain consists of 1) a near-source, small grid-size, rectangular structure of dimension 270 km $\times$ 50 km (black box area in Fig. S7a), and 2) a far-source homogeneous half-space (Fig. S7).

In the near-source region, we test different structural settings: a planar fault embedded in a homogeneous velocity structure and flat topography (Model 1 and Model 15); a curved fault embedded in a homogeneous velocity structure and flat topography (Model 2 and Model 16); and a curved fault embedded in a homogeneous velocity structure and realistic topography (Model 3 and Model 17). The rest of the models use a curved fault embedded in heterogeneous velocity structure and realistic topography. We use the P-wave velocity model directly from tomography (Miura et al., 2005). We use the empirical relation of Brocher (2005) to calculate density from the V_P values, $\rho = 1.74(V_P)^{0.25}$. The S-wave velocity V_S is calculated from a V_P/V_S ratio structure. For most of the simulation domain, we fix the V_P/V_S ratio constant of $\sqrt{3} \approx 1.73$, assuming a Poisson medium. For specific regions detailed as the blue outlined region in Fig. 2b (also see Figure S6), we raise the V_P/V_S ratio to the following values: 1.83 (Models 8 and 22), 1.94 (Models 9 and 23), 2.04 (Models 10 and 24), 2.14 (Models 11 and 25), 2.24 (Models 12 and 26), 2.34 (Models 13 and 27), and 2.45 (Models 14 and 28). For other heterogeneous models, the V_P/V_S ratio is fixed constant $\sqrt{3} \approx 1.73$ (Models 4-7 and Models 18-21). Finally, we can get the shear modulus $\mu = \rho V_S^2$.

For the homogeneous models in the far-source region, we have $V_P = 6.93$ km/s and $V_S = 4$ km/s, which are the same as those in the near-source region of Models 1-3 and 15-17. For the heterogeneous models, $V_P = 8.30$ km/s is chosen as the maximum P wave velocity in the model of Miura et al. (2005) and $V_S = 4.79$ km/s, corresponding to V_P/V_S ratio $= \sqrt{3}$. To avoid strong wave reflections from sharp velocity contrasts between the two simulation domains, we set a 5-km wide transition zone with a smooth gradient in the velocity values from the near-source to the far-source regions. At the boundaries of the simulation domain, we set the traction-free boundary condition on the top surface (blue line in Fig. S7), and absorbing boundary conditions along the borders of the semicircle domain (red line in Fig. S7).

As a benchmark case for the free-surface effects, we also run one model in a homogeneous full-space (no free surface, Model 29, also referred to as Full in the main text). The simulation domain of the full-space model is a sufficiently large circular domain with the same radius of 350 km, and an absorbing boundary condition encloses the entire domain. The same curved fault is embedded in the center of the simulation domain, and all other model parameters are kept identical to the homogeneous half-space model.

2.2. Friction

We use a linear slip weakening friction for most of our simulations (except Models 4-6 and 18-20). The parameters of linear slip weakening are constant from the surface down to 40 km depth (Supporting Information 2 (c)): static friction coefficient $\mu_s = 0.677$; dynamic friction coefficient $\mu_d = 0.2$; the critical slip of slip weakening $D_c = 0.4$ m. Below 40 km, we increase the dynamic friction coefficient to 0.99 to force the termination of the rupture. While the focus of this study is not to explore all frictional relations, we test several different friction relations above 10.8 km depth (at the base of the frontal prism) to be slip neutral/stable ($\mu_s = \mu_d = 0.677$ above 10.8 km depth, Models 4 and 18) or slip hardening/strengthening ($\mu_s = 0.677$, $\mu_s < \mu_d = 0.85$ and $D_c = 2$ m above 10.8 km depth, Models 5 and 19). Finally, we include a model with the same lab-based exponential slip weakening proposed by Murphy et al. (2018) in Models 6 and 20. We use the same relations (See their equations (1) and (2)) to set up the stress and frictional parameters.

2.3. Initial stress

In our simulations, the effective normal stress $\bar{\sigma}_n$ is reduced from the fault normal stress σ_L due to pore pressure p, $\bar{\sigma}_n = \sigma_L - p$. Because of the relatively low dip angle of the fault, we approximate the normal stress σ_L as the lithostatic stress that is calculated based on the density structure $\rho(x,h)$ of each model: $\sigma_L(x) = \int_{h_{slab}}^{h_0} \rho(x,h) g dh$, where h_{slab} and h_0 are the depths of slab surface and top free surface, g is the gravitation constant. We use the fluid pressure ratio λ to quantify the pore pressure: $p = \lambda \sigma_L$. This quantification is introduced by Hubbert and Rubey (1959) and has been used in many previous studies (e.g., Murphy et al., 2018; Lotto et al., 2018). Finally, we assume the effective normal stress $\bar{\sigma}_n$ is bounded at 40 MPa, at which the over-pressurized pore pressure becomes lithostatic (Rice, 1992), and this is similar to the settings in Lotto et al. (2018). In this study, we mainly vary λ for the stress setting variations of models and include cases of $\lambda = 0.9$ and $\lambda = 0.7$. This parameter controls how pore pressure varies along the depth and where the pore fluid becomes lithostatic (see Fig. 2c in the main text).

We assume a relatively low initial shear stress τ_0 on the fault and calculate it using the seismic S ratio (Fig. 2c), which is used to measure how close the initial stress is to the level of failure (Day, 1982):

$$S = \frac{\tau_s - \tau_0}{\tau_0 - \tau_d} = 2.77, \tag{1}$$

where $\tau_s = \bar{\sigma}_n \mu_s$ and $\tau_d = \bar{\sigma}_n \mu_d$ are the static friction (yielding stress) and dynamic friction, respectively. This high seismic S ratio is set to avoid the unwanted supershear rupture that arises from high initial stress and resulting high dynamic stress drop (Andrews, 1985; Dunham, 2007). Finally, we use over-stress nucleation to start the spontaneous dynamic rupture for all models. We increase the initial shear stress to $1.016\tau_s$ within a 2-km patch on fault centered at a depth of 20 km (Fig. 2c). The only exceptions are the models with exponential slip weakening friction (Models 6 and 20). We have to set a larger nucleation zone of about 14 km to nucleate megathrust rupture successfully. We have checked the results of those models (Models 6 and 20) and can assure that this large nucleation patch has negligible effects on the later dynamic rupture process.

2.4. Numerical solver

The entire domain is discretized with unstructured mesh using software CUBIT (`https://cubit.sandia.gov/`, the mesh script is written based on Huang, Meng, and Ampuero (2012)). To determine the element grid size, we estimate the corresponding cohesive zone size Λ_0 based on Palmer and Rice (1973): $\Lambda_0 = \frac{9\pi}{32}\frac{\mu}{(1-\nu)}\frac{D_c}{(\tau_s-\tau_d)}$, where $\nu = \frac{1}{2}\frac{(V_P/V_S)^2-2}{(V_P/V_S)^2-1}$ is the Poisson's ratio. For the homogeneous model $V_P = 6.93$ km/s, $V_P/V_S = \sqrt{3}$ and $\tau_s - \tau_d = 40$ MPa, the corresponding cohesive zone size $\Lambda_0 = 1114.4$ m. For the heterogeneous model, we take the case of $V_P = 4$ km/s, $V_P/V_S = 2.45$ and $\tau_s - \tau_d = 8$ MPa as a representative lower bond estimation, which gives the cohesive zone size $\Lambda_0 = 1012.6$ m. Based on the estimation of the cohesive zone size, we set the element grid size $dl = 500$ m $< \Lambda_0/2$ in the source domain (Fig. S7) to ensure sufficient numerical resolution (Day et al., 2005). Accordingly, the frequency resolution is determined by dl and the minimum S wave wavelength. We require at least $n = 4$ grids within the minimum wavelength, so we can estimate the maximum resolvable frequency of our simulations. This varies for different models. For the models with homogeneous velocity structure (Models 1-3, 15-17), $V_S = 4$ km/s and the maximum frequency we can resolve is $f = V_S/4dl = 2$ Hz. For the models with heterogeneous velocity structures, the maximum resolvable frequency varies with minimum V_S. The minimum shear wave speed in all the velocity models is 0.6 km/s, corresponding to $f = min(V_S)/4dl = 0.3$ Hz. In our results, we will interpret radiation below this maximum frequency. We use the 2D spectral element-based code SEM2DPACK (Ampuero, 2012, `https://github.com/jpampuero/sem2dpack`, last accessed on 06/08/2021) to solve for the dynamic rupture. This code has been well validated and applied in some previous studies (e.g., Huang & Ampuero, 2011; Huang et al., 2012) to simulate the megathrust earthquakes as well as the wave fields.

In most of our simulations, we include the realistic velocity models, which have significant material contrasts in the downdip regions (Fig. 2b or Fig. S6). The material contrasts can lead to ill-posedness in the numerical solution and regularization is needed (Cochard & Rice, 2000). As proposed by Rubin and Ampuero (2007); Ampuero and Ben-Zion (2008); Huang (2018), the material contrasts can cause normal stress perturbation during dynamic rupture. They suggest using a regularization $\dot{\sigma^*} = \frac{V^*}{D_\sigma}(\sigma - \sigma^*)$ to force the normal stress to evolve continuously. σ and σ^* are the actual normal stress and the regularized normal stress (referred to as an "effective" normal stress but here we use "regularized" to differentiate from the one related to pore pressure). The reference velocity V^* and slip distance D_σ are the two constitutive parameters. In our simulations, since we are focusing on the fault slip within the frequency band below 0.3 Hz, we apply a 1-s-long Gaussian window to smooth out the numerical noise in the slip rate functions. We compare models processed by different schemes and find that the slip-rate functions are almost indistinguishable (Fig. S13).

References

Agudelo, W., Ribodetti, A., Collot, J.-Y., & Operto, S. (2009). Joint inversion of multichannel seismic reflection and wide-angle seismic data: Improved imaging and refined velocity model of the crustal structure of the north Ecuador–south Colombia convergent margin. *Journal of Geophysical Research: Solid Earth*, *114*(B2). doi: https://doi.org/10.1029/2008JB005690

Ampuero, J. P. (2012). SEM2DPACK, a spectral element software for 2D seismic wave propagation and earthquake source dynamics, v2.3.8. Retrieved from https://doi.org/10.5281/zenodo.230363 (More information at https://github.com/jpampuero/sem2dpack) doi: 10.5281/zenodo.230363

Ampuero, J.-P., & Ben-Zion, Y. (2008). Cracks, pulses and macroscopic asymmetry of dynamic rupture on a bimaterial interface with velocity-weakening friction. *Geophysical Journal International*, *173*(2), 674–692. doi: 10.1111/j.1365-246X.2008.03736.x

Andrews, D. J. (1985). Dynamic plane-strain shear rupture with a slip-weakening friction law calculated by a boundary integral method. *Bulletin of the Seismological Society of America*, *75*(1), 1–21.

Bassett, D., Kopp, H., Sutherland, R., Henrys, S., Watts, A. B., Timm, C., … Ronde, C. E. J. d. (2016). Crustal structure of the Kermadec arc from MANGO seismic refraction profiles. *Journal of Geophysical Research: Solid Earth*, *121*(10), 7514–7546. doi: https://doi.org/10.1002/2016JB013194

Bassett, D., Sutherland, R., Henrys, S., Stern, T., Scherwath, M., Benson, A., … Henderson, M. (2010). Three-dimensional velocity structure of the northern Hikurangi margin, Raukumara, New Zealand: Implications for the growth of continental crust by subduction erosion and tectonic underplating. *Geochemistry, Geophysics, Geosystems*, *11*(10). doi: https://doi.org/10.1029/2010GC003137

Brocher, T. M. (2005). Empirical Relations between Elastic Wavespeeds and Density in the Earth's Crust. *Bulletin of the Seismological Society of America*, *95*(6), 2081–2092. doi: 10.1785/0120050077

Cochard, A., & Rice, J. R. (2000). Fault rupture between dissimilar materials: Ill-posedness, regularization, and slip-pulse response. *Journal of Geophysical Research: Solid Earth*, *105*(B11), 25891–25907. doi: https://doi.org/10.1029/2000JB900230

Contreras-Reyes, E., Becerra, J., Kopp, H., Reichert, C., & Díaz-Naveas, J. (2014). Seismic structure of the north-central Chilean convergent margin: Subduction erosion of a paleomagmatic arc. *Geophysical Research Letters*, *41*(5), 1523–1529. doi: https://doi.org/10.1002/2013GL058729

Contreras-Reyes, E., Grevemeyer, I., Flueh, E. R., & Reichert, C. (2008). Upper lithospheric structure of the subduction zone offshore of southern Arauco peninsula, Chile, at 38S. *Journal of Geophysical Research: Solid Earth*, *113*(B7). doi: https://doi.org/10.1029/2007JB005569

Contreras-Reyes, E., Grevemeyer, I., Watts, A. B., Flueh, E. R., Peirce, C., Moeller, S., & Papenberg, C. (2011). Deep seismic structure of the Tonga subduction zone: Implications for mantle hydration, tectonic erosion, and arc magmatism. *Journal of Geophysical Research: Solid Earth*, *116*(B10). doi: https://doi.org/10.1029/2011JB008434

Day, S. M. (1982). Three-dimensional simulation of spontaneous rupture: The effect of nonuniform prestress. *Bulletin of the Seismological Society of America*, *72*(6A), 1881–1902.

Day, S. M., Dalguer, L. A., Lapusta, N., & Liu, Y. (2005). Comparison of finite difference and boundary integral solutions to three-dimensional spontaneous rupture. *Journal of Geophysical Research: Solid Earth*, *110*(B12). doi: 10.1029/2005JB003813

Dunham, E. M. (2007). Conditions governing the occurrence of supershear ruptures under slip-weakening friction. *Journal of Geophysical Research: Solid Earth*, *112*(B7). doi: 10.1029/2006JB004717

Gailler, A., Charvis, P., & Flueh, E. R. (2007). Segmentation of the Nazca and South American plates along the Ecuador subduction zone from wide angle seismic profiles. *Earth and Planetary Science Letters*, *260*(3), 444–464. doi: 10.1016/j.epsl.2007.05.045

Graindorge, D., Calahorrano, A., Charvis, P., Collot, J.-Y., & Bethoux, N. (2004). Deep structures of the Ecuador convergent margin and the Carnegie Ridge, possible consequence on great earthquakes recurrence interval. *Geophysical Research Letters*, *31*(4). doi: https://doi.org/10.1029/2003GL018803

Hampel, A., Kukowski, N., Bialas, J., Huebscher, C., & Heinbockel, R. (2004). Ridge subduction at an erosive margin: The collision zone of the Nazca Ridge in southern Peru. *Journal of Geophysical Research: Solid Earth*, *109*(B2). doi: https://doi.org/10.1029/2003JB002593

Hayes, G. P., Moore, G. L., Portner, D. E., Hearne, M., Flamme, H., Furtney, M., & Smoczyk, G. M. (2018). Slab2, a comprehensive subduction zone geometry model. *Science*, *362*(6410), 58–61. doi: 10.1126/science.aat4723

Horning, G., Canales, J. P., Carbotte, S. M., Han, S., Carton, H., Nedimović, M. R., & Keken, P. E. v. (2016). A 2-D tomographic model of the Juan de Fuca plate from accretion at axial seamount to subduction at the Cascadia margin from an active source ocean bottom seismometer survey. *Journal of Geophysical Research: Solid Earth*, *121*(8), 5859–5879. doi: https://doi.org/10.1002/2016JB013228

Huang, Y. (2018). Earthquake Rupture in Fault Zones With Along-Strike Material Heterogeneity. *Journal of Geophysical Research: Solid Earth*, *123*(11), 9884–9898. doi: https://doi.org/10.1029/2018JB016354

Huang, Y., & Ampuero, J.-P. (2011). Pulse-like ruptures induced by low-velocity fault zones. *Journal of Geophysical Research: Solid Earth*, *116*(B12). doi: 10.1029/2011JB008684

Huang, Y., Meng, L., & Ampuero, J.-P. (2012). A dynamic model of the frequency-dependent rupture process of the 2011 Tohoku-Oki earthquake. *Earth, Planets and Space*, *64*(12), 1. doi: 10.5047/eps.2012.05.011

Hubbert, M. K., & Rubey, W. W. (1959). Role of fluid pressure in mechanics of overthrust faulting: I. mechanics of fluid-filled porous solids and its application to overthrust faulting. *GSA Bulletin*, *70*(2), 115–166. doi: 10.1130/0016-7606(1959)70[115:ROFPIM]2.0.CO;2

Incorporated Research Institutions for Seismology Data Management Center. (2011). Data Services Products: BackProjection P-wave back-projection rupture imaging. doi: 10.17611/DP/BP.1.

Klingelhoefer, F., Berthet, T., Lallemand, S., Schnurle, P., Lee, C. S., Liu, C. S., ... Theunissen, T. (2012). P-wave velocity structure of the southern Ryukyu margin east of Taiwan: Results from the ACTS wide-angle seismic experiment. *Tectonophysics*, *578*, 50–62. doi: 10.1016/j.tecto.2011.10.010

Klingelhoefer, F., Gutscher, M.-A., Ladage, S., Dessa, J.-X., Graindorge, D., Franke, D., ... Chauhan, A. (2010). Limits of the seismogenic zone in the epicentral region of the 26 December 2004 great Sumatra-Andaman earthquake: Results from seismic refraction and wide-angle reflection surveys and thermal modeling. *Journal of Geophysical Research: Solid Earth*, *115*(B1). doi: https://doi.org/10.1029/2009JB006569

Kodaira, S., Takahashi, N., Park, J.-O., Mochizuki, K., Shinohara, M., & Kimura, S. (2000). Western Nankai Trough seismogenic zone: Results from a wide-angle ocean bottom seismic survey. *Journal of Geophysical Research: Solid Earth*, *105*(B3), 5887–5905. doi: https://doi.org/10.1029/1999JB900394

Kopp, H., Weinzierl, W., Becel, A., Charvis, P., Evain, M., Flueh, E. R., ... Roux, E. (2011). Deep structure of the central Lesser Antilles Island Arc: Relevance for the formation of continental crust. *Earth and Planetary Science Letters*, *304*(1), 121–134. doi: 10.1016/j.epsl.2011.01.024

Krabbenhöft, A., Bialas, J., Kopp, H., Kukowski, N., & Hübscher, C. (2004). Crustal structure of the Peruvian continental margin from wide-angle seismic studies. *Geophysical Journal International*, *159*(2), 749–764. doi: 10.1111/j.1365-246X.2004.02425.x

Lay, T., Kanamori, H., Ammon, C. J., Koper, K. D., Hutko, A. R., Ye, L., ... Rushing, T. M. (2012). Depth-varying rupture properties of subduction zone megathrust faults. *Journal of Geophysical Research: Solid Earth*, *117*(B4), B04311. doi: 10.1029/2011JB009133

Lotto, G. C., Jeppson, T. N., & Dunham, E. M. (2018). Fully Coupled Simulations of Megathrust Earthquakes and Tsunamis in the Japan Trench, Nankai Trough, and Cascadia Subduction Zone. *Pure and Applied Geophysics*. doi: 10.1007/s00024-018-1990-y

Martínez-Loriente, S., Sallarès, V., Ranero, C. R., Ruh, J. B., Barckhausen, U., Grevemeyer, I., & Bangs, N. (2019). Influence of Incoming Plate Relief on Overriding Plate Deformation and Earthquake Nucleation: Cocos Ridge Subduction (Costa Rica). *Tectonics*, *38*(12), 4360–4377. doi: https://doi.org/10.1029/2019TC005586

Miura, S., Suyehiro, K., Shinohara, M., Takahashi, N., Araki, E., & Taira, A. (2004). Seismological structure and implications of collision between the Ontong Java Plateau and Solomon Island Arc from ocean bottom seismometer–airgun data. *Tectonophysics*, *389*(3), 191–220. doi: 10.1016/j.tecto.2003.09.029

Miura, S., Takahashi, N., Nakanishi, A., Tsuru, T., Kodaira, S., & Kaneda, Y. (2005). Structural characteristics off Miyagi forearc region, the Japan Trench seismogenic zone, deduced from a wide-angle reflection and refraction study. *Tectonophysics*, *407*(3), 165–188. doi: 10.1016/j.tecto.2005.08.001

Moscoso, E., Grevemeyer, I., Contreras-Reyes, E., Flueh, E. R., Dzierma, Y., Rabbel, W., & Thorwart, M. (2011). Revealing the deep structure and rupture plane of the 2010 Maule, Chile earthquake (Mw=8.8) using wide angle seismic data. *Earth and Planetary Science Letters*, *307*(1), 147–155. doi: 10.1016/j.epsl.2011.04.025

Murphy, S., Di Toro, G., Romano, F., Scala, A., Lorito, S., Spagnuolo, E., ... Nielsen, S. (2018). Tsunamigenic earthquake simulations using experimentally derived friction laws. *Earth and Planetary Science Letters*, *486*, 155–165. doi: 10.1016/j.epsl.2018.01.011

Nakanishi, A., Kurashimo, E., Tatsumi, Y., Yamaguchi, H., Miura, S., Kodaira, S., ... Hirata, N. (2009). Crustal evolution of the southwestern Kuril Arc, Hokkaido Japan, deduced from seismic velocity and geochemical structure. *Tectonophysics*, *472*(1), 105–123. doi: 10.1016/j.tecto.2008.03.003

Nakanishi, A., Takahashi, N., Park, J.-O., Miura, S., Kodaira, S., Kaneda, Y., ... Nakamura, M. (2002). Crustal structure across the coseismic rupture zone of the 1944 Tonankai earthquake, the central Nankai Trough seismogenic zone. *Journal of Geophysical Research: Solid Earth*, *107*(B1), EPM 2–1–EPM 2–21. doi: https://doi.org/10.1029/2001JB000424

Nishizawa, A., Kaneda, K., Oikawa, M., Horiuchi, D., Fujioka, Y., & Okada, C. (2017). Variations in seismic velocity distribution along the Ryukyu (Nansei-Shoto) Trench subduction zone at the northwestern end of the Philippine Sea plate. *Earth, Planets and Space*, *69*(1), 86. doi: 10.1186/s40623-017-0674-7

Palmer, A. C., & Rice, J. R. (1973). The growth of slip surfaces in the progressive failure of over-consolidated clay. *Proceedings of the Royal Society of London. A. Mathematical and Physical Sciences*, *332*(1591), 527–548. doi: 10.1098/rspa.1973.0040

Planert, L., Kopp, H., Lueschen, E., Mueller, C., Flueh, E. R., Shulgin, A., … Krabbenhoeft, A. (2010). Lower plate structure and upper plate deformational segmentation at the Sunda-Banda arc transition, Indonesia. *Journal of Geophysical Research: Solid Earth*, *115*(B8). doi: https://doi.org/10.1029/2009JB006713

Rice, J. R. (1992). Chapter 20 Fault Stress States, Pore Pressure Distributions, and the Weakness of the San Andreas Fault. In B. Evans & T.-f. Wong (Eds.), *International Geophysics* (Vol. 51, pp. 475–503). Academic Press. doi: 10.1016/S0074-6142(08)62835-1

Rubin, A. M., & Ampuero, J.-P. (2007). Aftershock asymmetry on a bimaterial interface. *Journal of Geophysical Research: Solid Earth*, *112*(B5). doi: https://doi.org/10.1029/2006JB004337

Sallarès, V., Dañobeitia, J. J., & Flueh, E. R. (2001). Lithospheric structure of the Costa Rican Isthmus: Effects of subduction zone magmatism on an oceanic plateau. *Journal of Geophysical Research: Solid Earth*, *106*(B1), 621–643. doi: https://doi.org/10.1029/2000JB900245

Scherwath, M., Contreras-Reyes, E., Flueh, E. R., Grevemeyer, I., Krabbenhoeft, A., Papenberg, C., … Weinrebe, R. W. (2009). Deep lithospheric structures along the southern central Chile margin from wide-angle P-wave modelling. *Geophysical Journal International*, *179*(1), 579–600. doi: 10.1111/j.1365-246X.2009.04298.x

Shulgin, A., Kopp, H., Mueller, C., Planert, L., Lueschen, E., Flueh, E. R., & Djajadihardja, Y. (2011). Structural architecture of oceanic plateau subduction offshore Eastern Java and the potential implications for geohazards. *Geophysical Journal International*, *184*(1), 12–28. doi: 10.1111/j.1365-246X.2010.04834.x

Takahashi, N., Suyehiro, K., & Shinohara, M. (1998). Implications from the seismic crustal structure of the northern Izu–Bonin arc. *Island Arc*, *7*(3), 383–394. doi:

https://doi.org/10.1111/j.1440-1738.1998.00197.x

Walther, C. H. E., Flueh, E. R., Ranero, C. R., Von Huene, R., & Strauch, W. (2000). Crustal structure across the Pacific margin of Nicaragua:evidence for ophiolitic basement and a shallow mantle sliver. *Geophysical Journal International*, *141*(3), 759–777. doi: 10.1046/j.1365-246x.2000.00134.x

Wang, D., & Mori, J. (2011). Frequency-dependent energy radiation and fault coupling for the 2010 Mw8.8 Maule, Chile, and 2011 Mw9.0 Tohoku, Japan, earthquakes. *Geophysical Research Letters*, *38*(22). doi: 10.1029/2011GL049652

Yao, H., Gerstoft, P., Shearer, P. M., & Mecklenbräuker, C. (2011). Compressive sensing of the Tohoku-Oki Mw 9.0 earthquake: Frequency-dependent rupture modes. *Geophysical Research Letters*, *38*(20), L20310. doi: 10.1029/2011GL049223

Ye, S., Flueh, E. R., Klaeschen, D., & von Huene, R. (1997). Crustal structure along the EDGE transect beneath the Kodiak shelf off Alaska derived from OBH seismic refraction data. *Geophysical Journal International*, *130*(2), 283–302. doi: 10.1111/j.1365-246X.1997.tb05648.x

Yin, J., & Denolle, M. A. (2019). Relating teleseismic backprojection images to earthquake kinematics. *Geophysical Journal International*, *217*(2), 729–747. doi: 10.1093/gji/ggz048

Yin, J., Denolle, M. A., & Yao, H. (2018). Spatial and Temporal Evolution of Earthquake Dynamics: Case Study of the Mw 8.3 Illapel Earthquake, Chile. *Journal of Geophysical Research: Solid Earth*, *123*(1), 344–367. doi: 10.1002/2017JB014265

Yin, J., Yang, H., Yao, H., & Weng, H. (2016). Coseismic radiation and stress drop during the 2015 Mw 8.3 Illapel, Chile megathrust earthquake. *Geophysical Research Letters*, *43*(4), 1520–1528. doi: 10.1002/2015GL067381

Yin, J., Yao, H., Yang, H., Qin, W., Jing, L.-Z., & Zhang, H. (2017). Frequency-dependent rupture process, stress change, and seismogenic mechanism of the 25 April 2015 Nepal Gorkha Mw 7.8 earthquake. *SCIENCE CHINA Earth Sciences*, *60*(4), 796–808. doi: 10.1007/s11430-016-9006-0

Zhu, J., Kopp, H., Flueh, E. R., Klaeschen, D., Papenberg, C., & Planert, L. (2009). Crustal structure of the central Costa Rica subduction zone: Implications for basal erosion from seismic wide-angle data. *Geophysical Journal International*, *178*(2), 1112–1131. doi: 10.1111/j.1365-246X.2009.04208.x

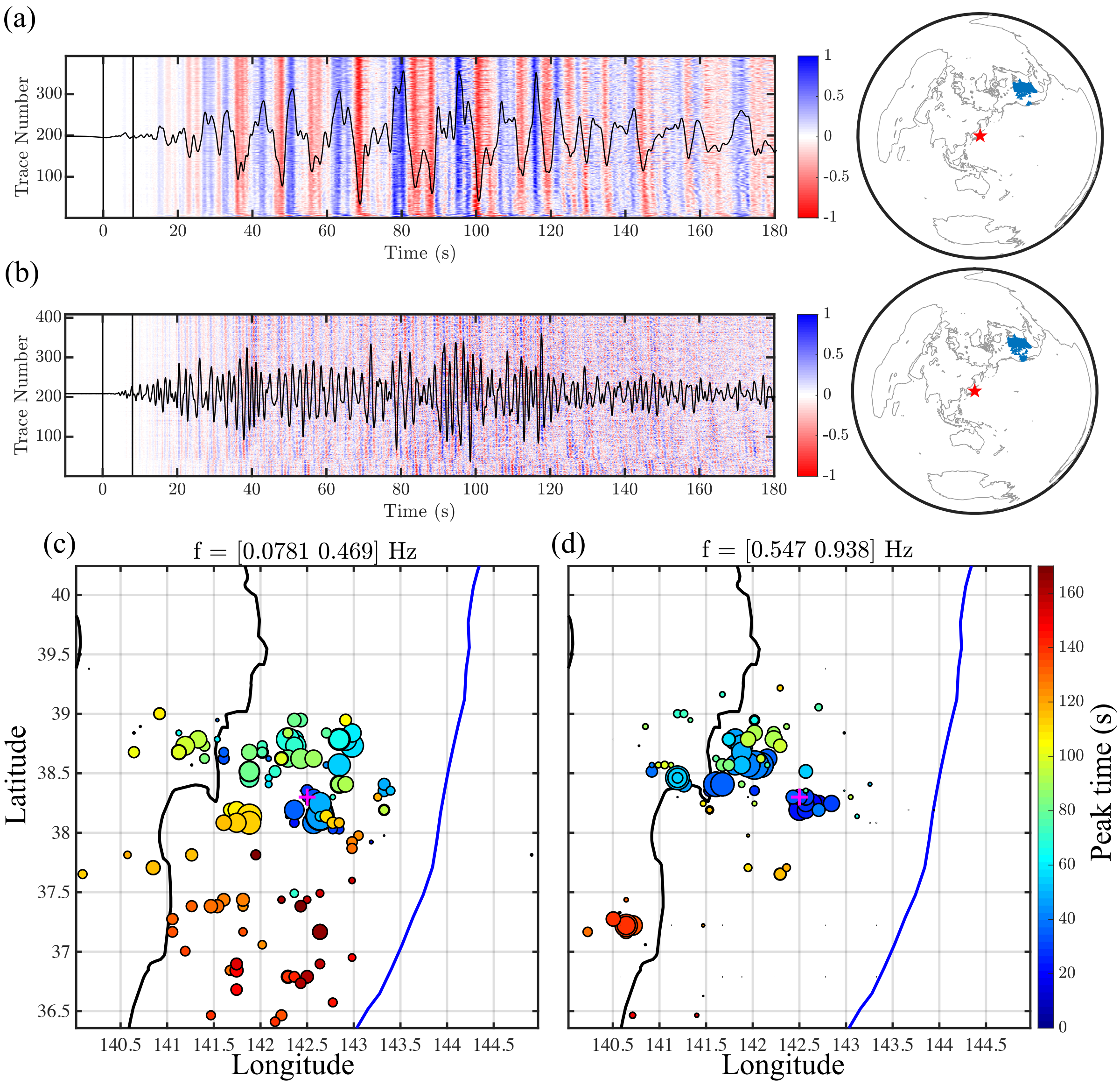

Figure S1: Data and back-projection results of the Mw 9.0 2011 Tohoku-oki earthquake. (a) Teleseismic P wave velocity seismograms filtered in the LF band (0.05 - 0.5 Hz) and the corresponding TA array distribution (blue triangles to the right and the red star indicates the location of the epicenter). The aligned waveforms recorded by the array are shown by the red-to-blue image and the stacked waveform is also shown on top of the image. (b) Same as (a) but for the teleseismic P wave velocity seismograms filtered in the high-frequency band (0.5 - 1 Hz). (c) imCS-BP results in the low-frequency band (0.05 - 0.5 Hz): the circles indicate the energy bursts, their colors correspond to the time of the burst since the onset of the earthquake, and their sizes are proportional to the amplitude power of energy bursts. The purple cross indicates the location of the epicenter. (d) The imCS-BP results in the high-frequency band (0.5 - 1 Hz) and the symbols have the same meanings as (c).

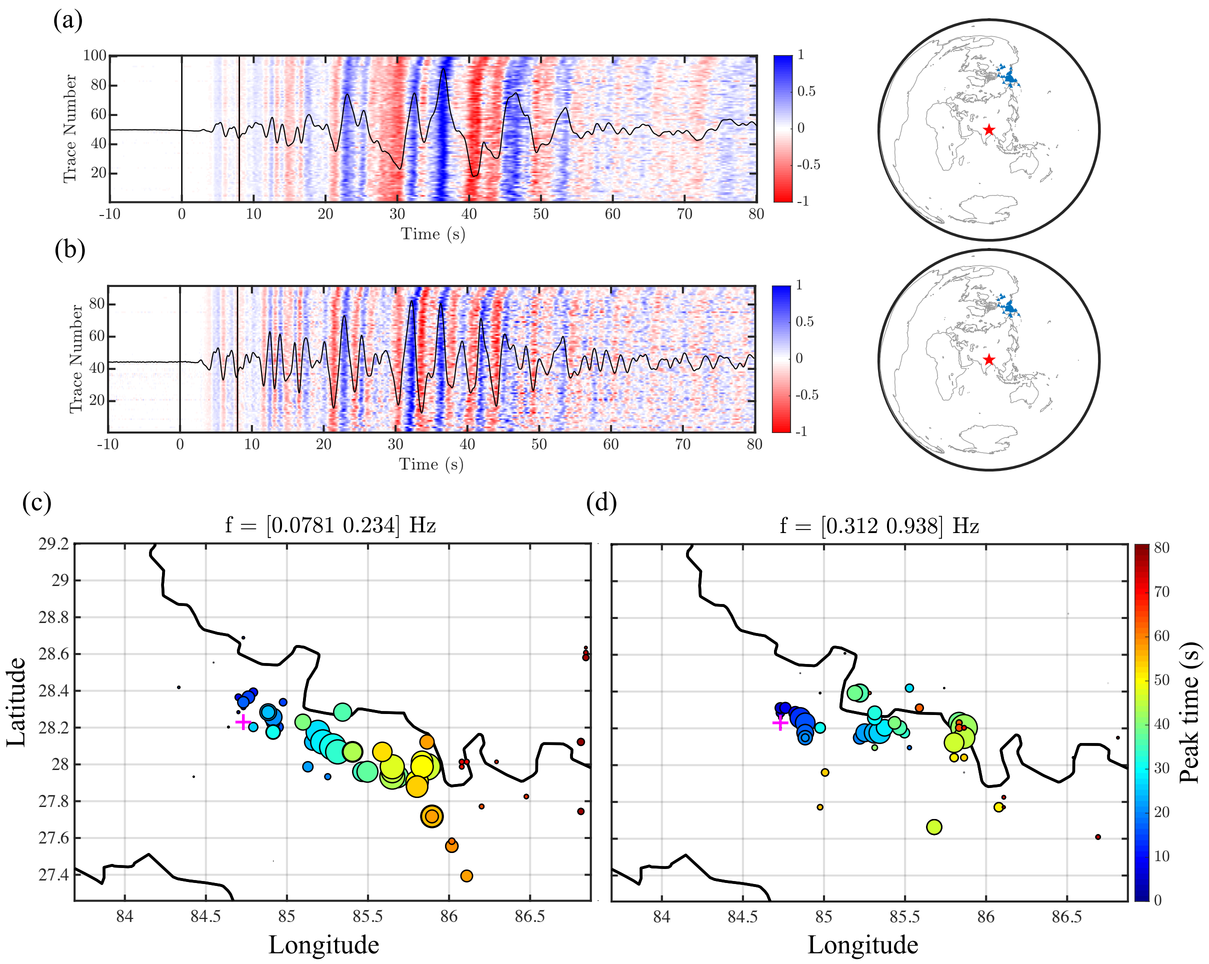

Figure S2: Data and back-projection results of the Mw 7.9 2015 Gorkha earthquake. (a) Teleseismic P-wave velocity seismograms filtered in the low-frequency band (0.05 - 0.25 Hz). (b) Same as (a) but for the teleseismic P-wave velocity seismograms filtered in the high-frequency band (0.25 - 1 Hz). (c) imCS-BP results in the low-frequency band (0.05 - 0.25 Hz). (d) imCS-BP results in the high-frequency band (0.25 - 1 Hz) and all other symbols have the same meanings as Fig. S1.

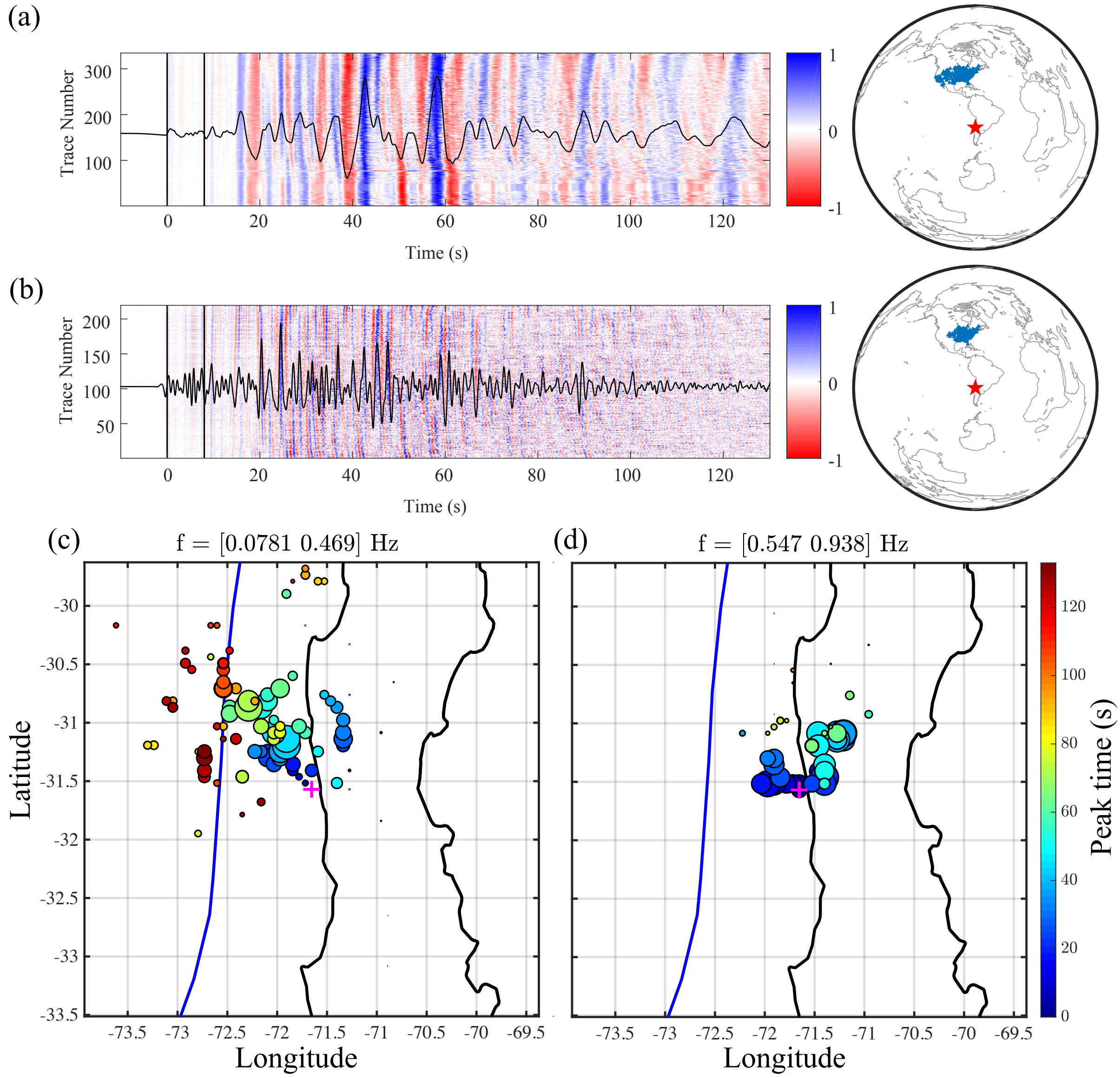

Figure S3: Data and back-projection results of the Mw 8.3 2015 Illapel earthquake. (a) Teleseismic P-wave velocity seismograms filtered in the LF band (0.05 - 0.5 Hz). (b) Same as (a) but for the teleseismic P-wave velocity seismograms filtered in the high-frequency band (0.5 - 1 Hz). (c) imCS-BP results in the low-frequency band (0.05 - 0.5 Hz). (d) imCS-BP results in the high-frequency band (0.5 - 1 Hz) and all other symbols have the same meanings as Fig. S1.

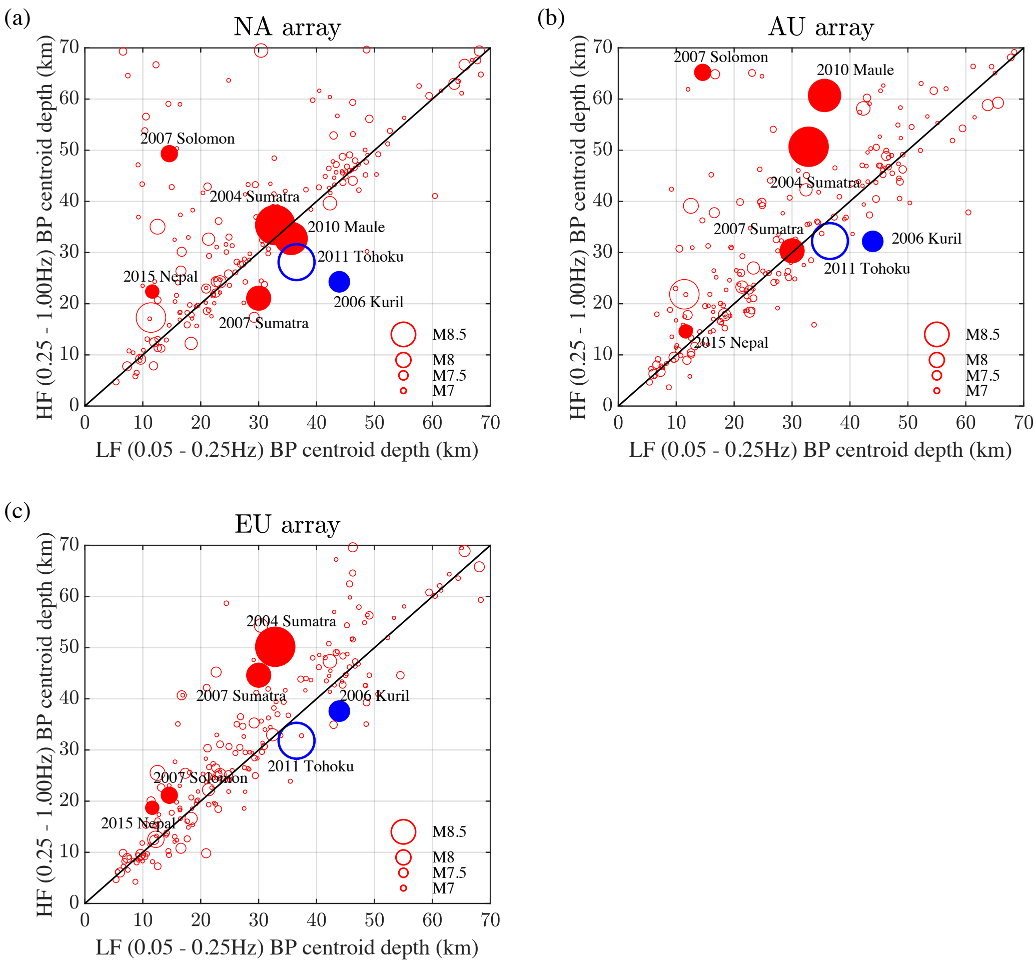

Figure S4: Comparison between the LF BP centroid depth from GSN and HF BP centroid depth from (a) North America NA array; (b) Australian AU array and (c) European EU array for the megathrust earthquakes in the IRIS back-projection database.

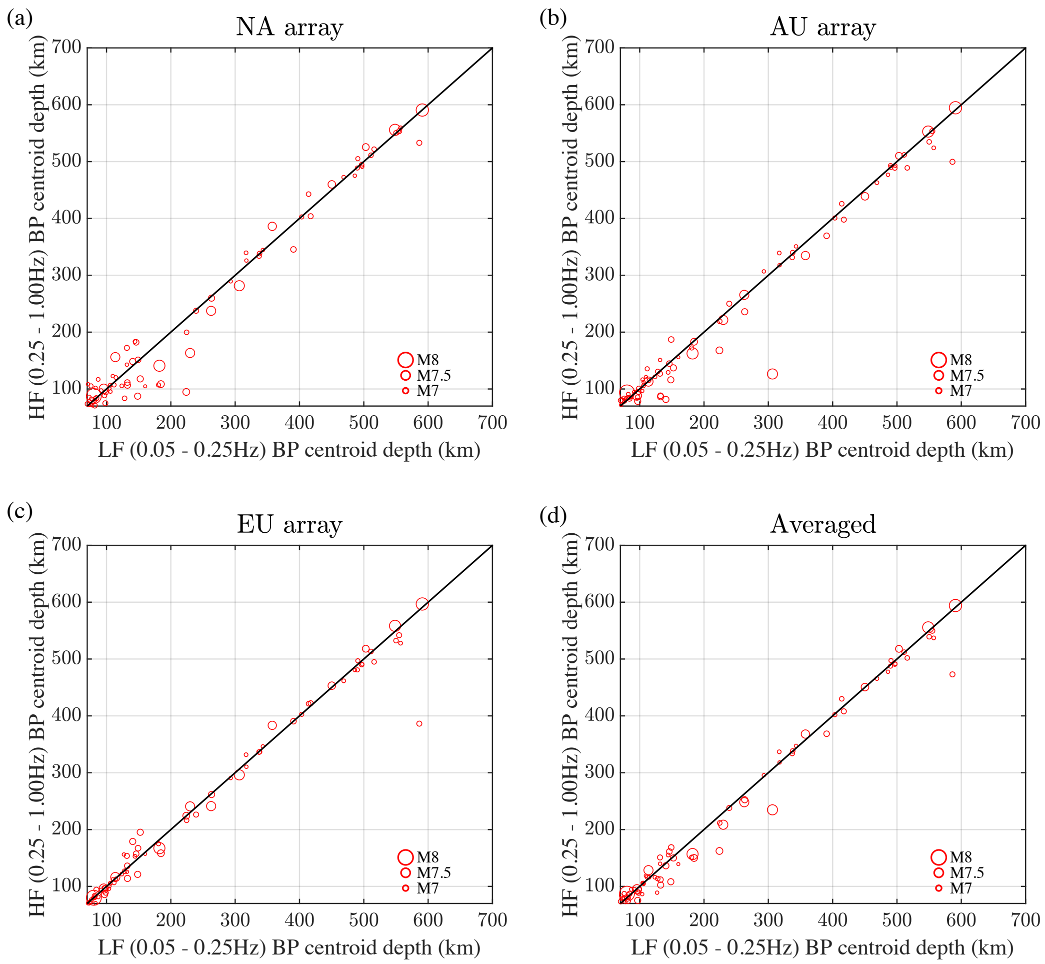

Figure S5: Comparison between the LF BP centroid depth from GSN and HF BP centroid depth from (a) NA array; (b) AU array; (c) EU array and (d) three-array-average for the deep earthquakes (70 - 700 km) in the IRIS back-projection database.

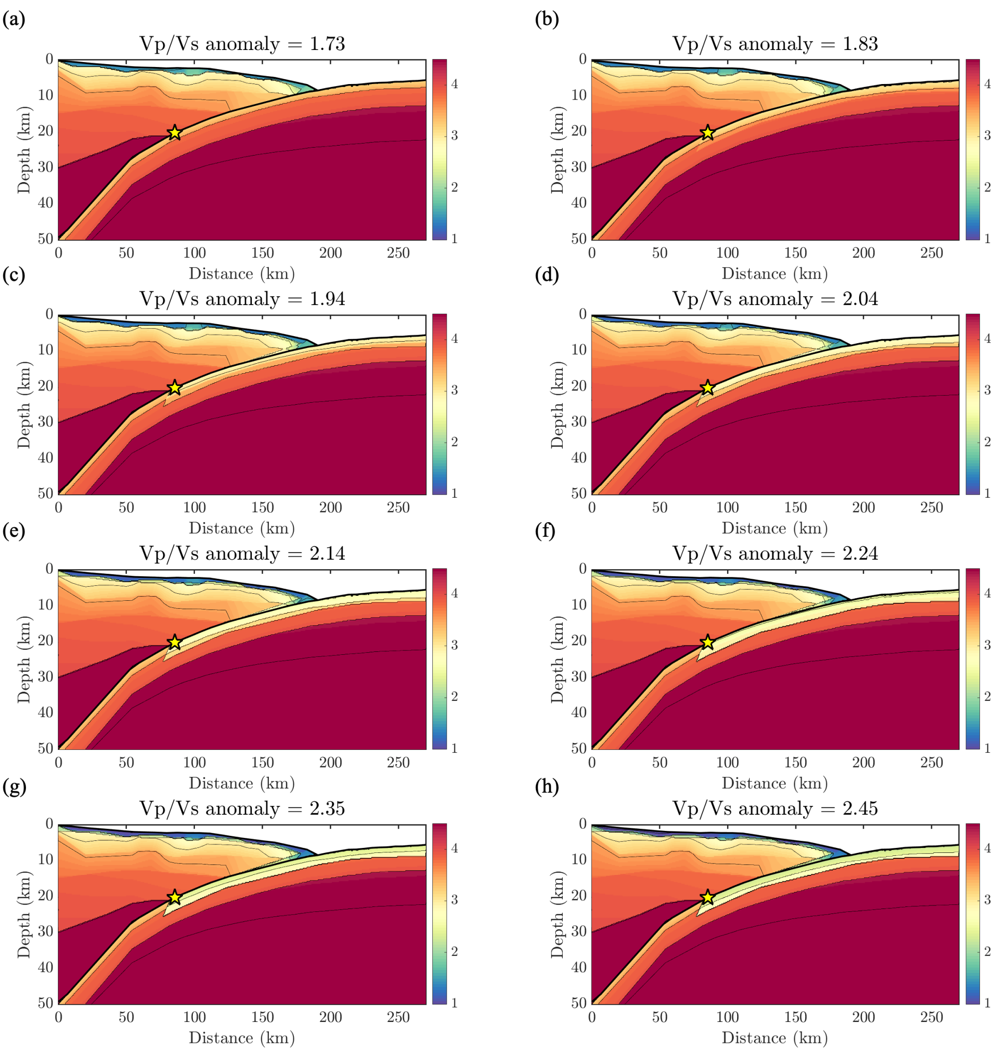

Figure S6: Corresponding S wave velocity from different settings of V_P/V_S ratios: (a) $V_P/V_S = 1.73$; (b) $V_P/V_S = 1.84$; (c) $V_P/V_S = 1.94$; (d) $V_P/V_S = 2.04$; (e) $V_P/V_S = 2.14$; (f) $V_P/V_S = 2.24$; (g) $V_P/V_S = 2.34$; (h) $V_P/V_S = 2.45$.

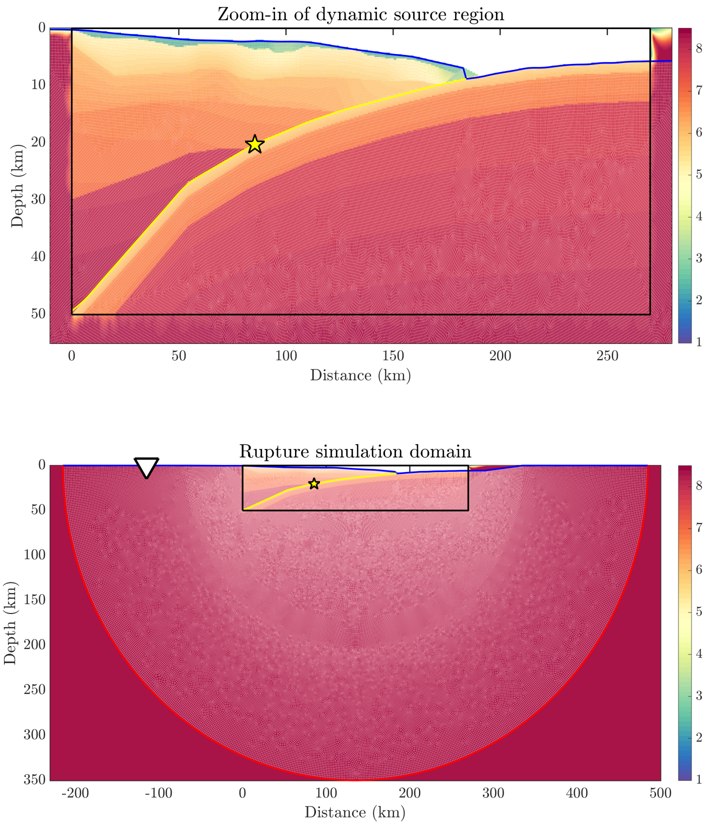

Figure S7: **Domain of dynamic simulations**. (top) The near-source region with various model settings: Blue and yellow lines indicate the free surface and dynamic fault, respectively. The colormap shows the P wave velocity from Miura et al. (2005). The star indicates the hypocenter of simulated megathrust earthquakes. (bottom) Entire simulation domain: The red semicircle indicates the domain boundary with absorbing conditions. The unstructured mesh is shown in white on top of the simulation domain.

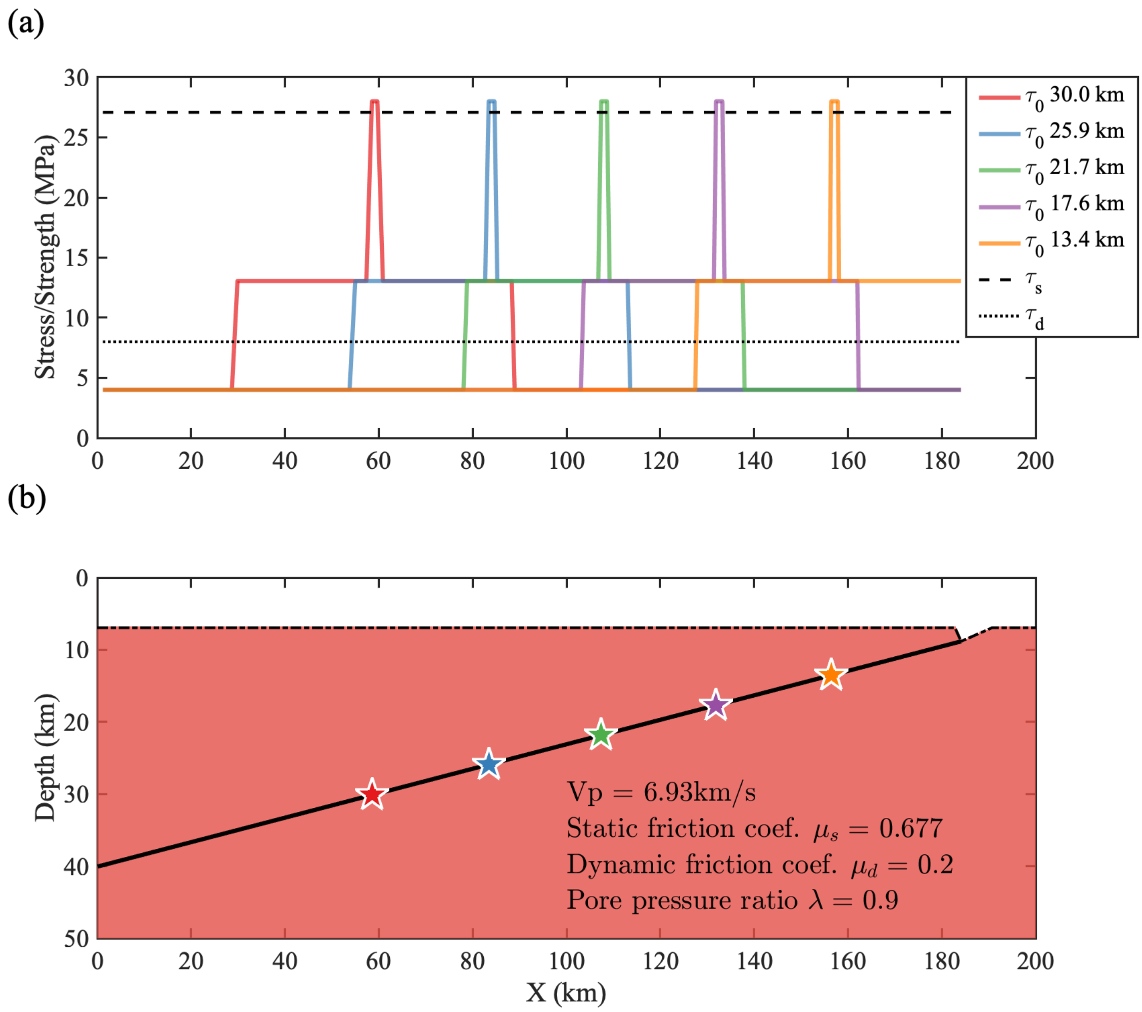

Figure S8: **Model settings of the five small megathrust earthquake models**. (a) Stress/strength distribution along the slab (in X coordinate): the black dotted line and dashed line show the dynamic friction τ_d and static friction τ_s, respectively. Colored lines indicate the initial shear stress τ_0 for earthquakes nucleated at different depths: red - 30.0 km; blue - 25.9 km; green - 21.7 km; purple - 17.6 km; orange - 13.4 km. (b) Simulation domain for a homogeneous medium with planar slab geometry and flat topography for the small rupture models. The colored stars indicate the location of nucleation/hypocenters of the small earthquakes.

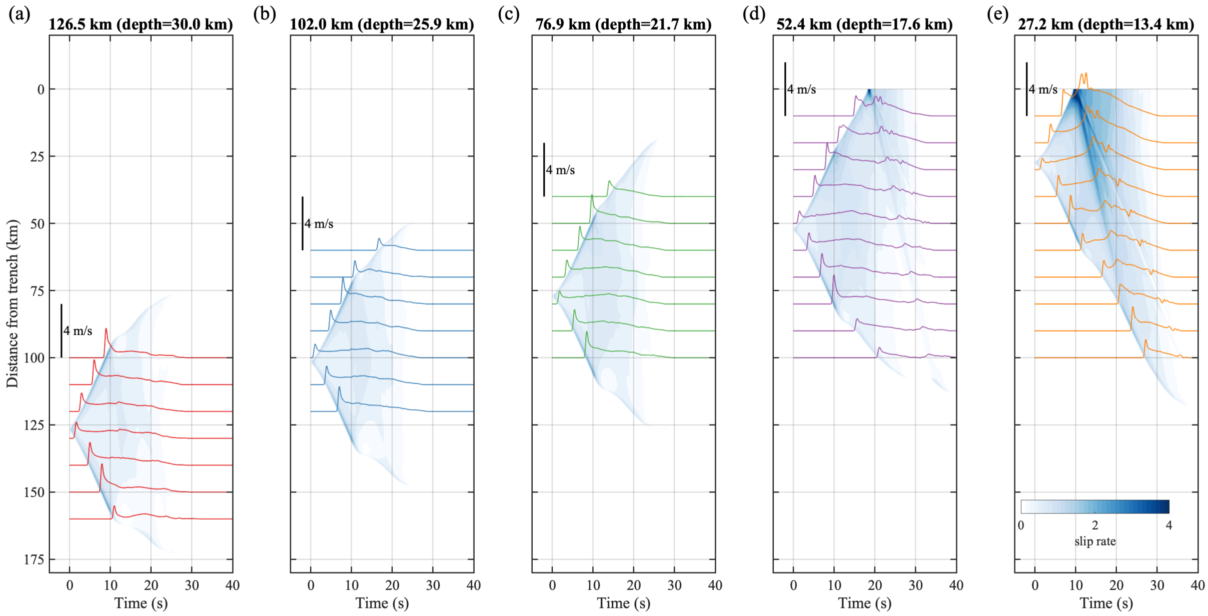

Figure S9: Space-time plot of the slip histories for all small earthquake models nucleated at different depths measured by distance from trench (depth): (a) distance = 126.5 km / depth = 30.0 km; (b) distance = 102.0 km / depth = 25.9 km; (c) distance = 76.9 km/ depth = 21.7 km; (d) distance = 52.4 km / depth = 17.6 km and (e) distance = 27.2 km / depth = 13.4km. The slip-rate functions at different points are also shown in colored lines.

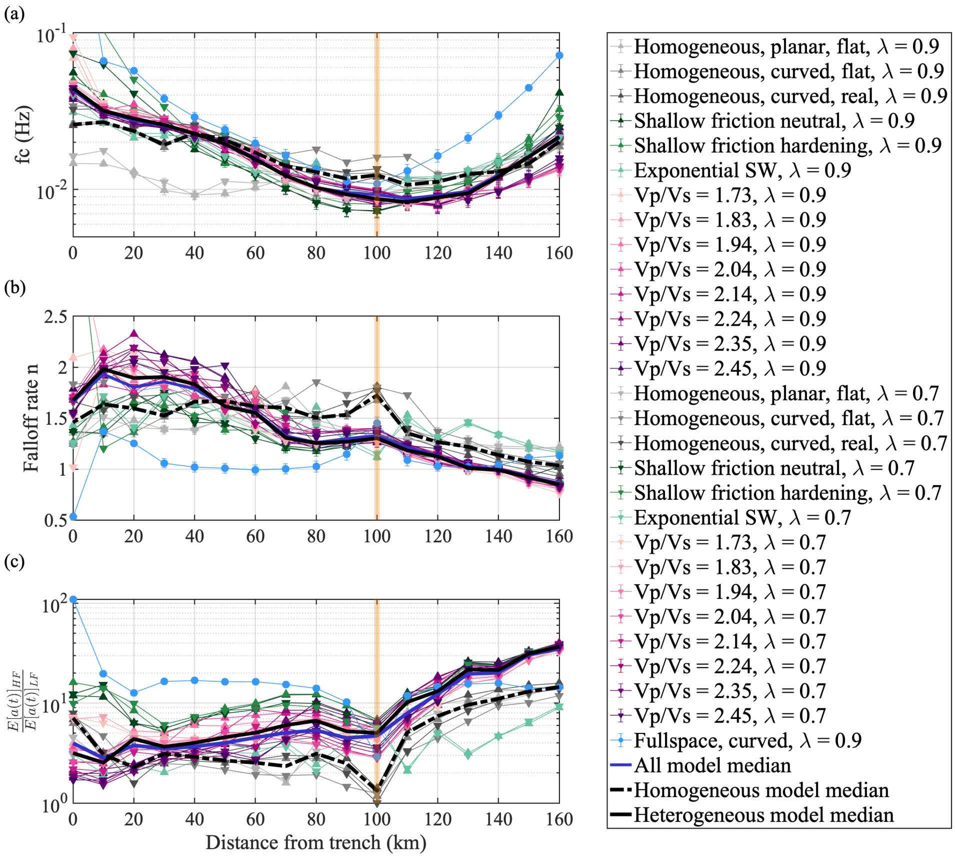

Figure S10: Results of the spectral content of the **slip-rate function extracted at individual point every 10 km** along dip: (a) corner frequency f_c; (b) spectral falloff rate n; (c) HF/LF power ratio of slip acceleration. Yellow bars indicate the location where rupture is nucleated.

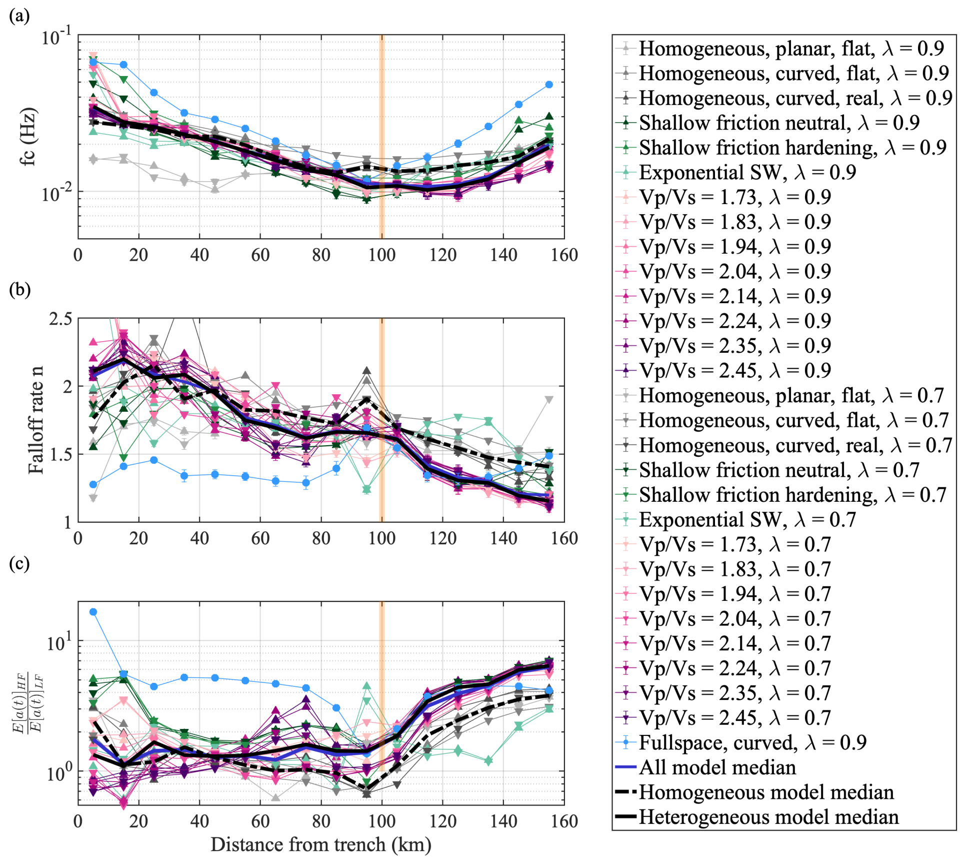

Figure S11: Results of the spectral content of the **slip-rate functions averaged over 10-km subfault** along dip: (a) corner frequency f_c; (b) spectral falloff rate n; (c) HF/LF power ratio of slip acceleration. Yellow bars indicate the location where rupture is nucleated.

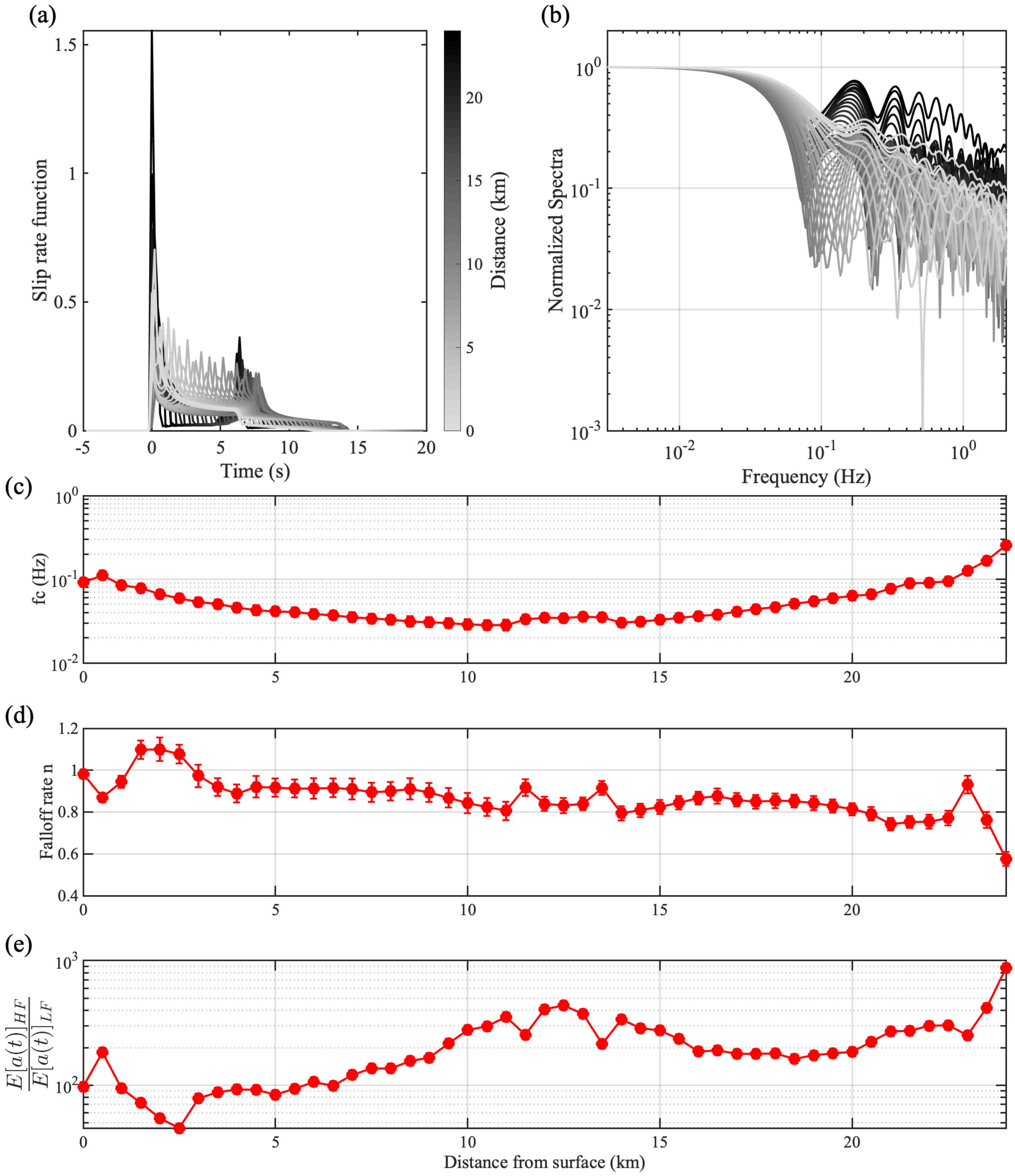

Figure S12: Results of a mode-III (anti-plane) rupture model on a vertical fault intersecting the free surface in a homogeneous medium. Fault length is 25 km, and the rupture is nucleated at 12.5 km depth with over-stress nucleation. Other model parameters are: V_P=6.9 km/s, V_S=4.0 km/s, D_c=0.4 m, μ_S=0.677, μ_D=0.2, $\bar{\sigma}_n$=40 MPa. (a) - (b) Slip-rate function and slip-rate spectrum at different depths. (c) - (e) Along-depth variation of corner frequency f_c, spectral falloff rate n and HF/LF power ratio of slip acceleration.

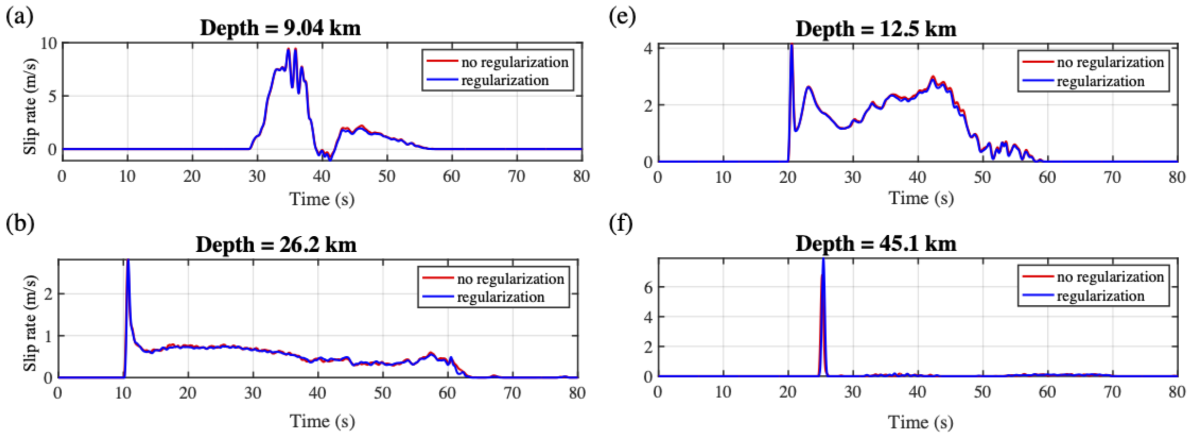

Figure S13: Comparisons between slip-rate functions with (blue) or without (red) normal stress regularization after the Gaussian time window smoothing, extracted at different depths: (a) 9.04 km; (b) 12.5 km; (c) 26.2 km and (d) 45.1 km.

Table S1: Range in V_P values in the downgoing slab low velocity zone LVZ (V_{LVZ}) and in the overhanging continental crust (V_{cont}) for various subduction zones.

Subduction zone	Reference	V_{LVZ} (km/s)	V_{cont} (km/s)
Alaska	Ye, Flueh, Klaeschen, and von Huene (1997)	4.9 - 5.1	4.6 - 5.1
Antilles	Kopp et al. (2011)	5.5 - 6.0	6.5 - 8.0
Cascadia	Horning et al. (2016)	4.0 - 4.5	4.5 - 6.5
Chile 1	Contreras-Reyes, Grevemeyer, Flueh, and Reichert (2008)	3.5 - 4.8	5.5 - 6.0
Chile 2	Scherwath et al. (2009)	4.5 - 5.0	5.0 - 7.0
Chile 3	Moscoso et al. (2011)	4.5 - 6.0	6.0 - 6.9
Chile 4	Contreras-Reyes, Becerra, Kopp, Reichert, and Díaz-Naveas (2014)	4.0 - 5.0	5.5 - 7.0
Costa Rica 1	Walther, Flueh, Ranero, Von Huene, and Strauch (2000)	5.5 - 6.0	5.7 - 8.3
Costa Rica 2	Sallarès, Dañobeitia, and Flueh (2001)	5.0 - 6.3	5.9 - 7.2
Costa Rica 3	Zhu et al. (2009)	3.0 - 4.0	4.5 - 6.0
Costa Rica 4	Martínez-Loriente et al. (2019)	4.0 - 5.0	4.0 - 6.5
Ecuador 1	Graindorge, Calahorrano, Charvis, Collot, and Bethoux (2004)	5.0 - 6.0	6.0 - 6.7
Ecuador 2	Gailler, Charvis, and Flueh (2007)	4.5 - 6.0	4.5 - 6.5
Ecuador 3	Agudelo, Ribodetti, Collot, and Operto (2009)	4.5 - 6.0	6.0 - 7.0
Izu Bonin	Takahashi, Suyehiro, and Shinohara (1998)	4.7 - 6.4	5.7 - 7.4
Java 1	Planert et al. (2010)	3.0 - 4.5	5.0 - 7.6
Java 2	Shulgin et al. (2011)	5.0 - 6.0	5.0 - 7.5
Kuril	Nakanishi et al. (2009)	4.5 - 6.0	6.0 - 8.0
Nankai Trough 1	Kodaira et al. (2000)	5.2 - 5.8	5.2 - 6.7
Nankai Trough 2	Nakanishi et al. (2002)	4.2 - 5.4	5.0 - 6.8
New Zealand	Bassett et al. (2010)	4.9 - 6.3	6.8 - 8.5
Nicaragua 1	Walther et al. (2000)	5.5 - 6.9	5.9 - 8.3
Peru 1	Hampel, Kukowski, Bialas, Huebscher, and Heinbockel (2004)	4.5 - 5.0	4.2 - 5.5
Peru 2	Krabbenhöft, Bialas, Kopp, Kukowski, and Hübscher (2004)	4.0 - 6.1	5.7 - 6.5
Ryukyu	Nishizawa et al. (2017)	5.0 - 6.0	5.0 - 7.0
Sumatra	Klingelhoefer et al. (2010)	5.0 - 6.0	5.0 - 8.0
Solomon	Miura et al. (2004)	5.0 - 6.3	5.3 - 6.9
Taiwan	Klingelhoefer et al. (2012)	5.5 - 6.0	4.5 - 7.0
Tohoku	Miura et al. (2005)	5.5 - 6.6	5.5 - 8.0
Tonga 1	Contreras-Reyes et al. (2011)	5.5 - 6.5	6.0 - 7.5
Tonga 2	Bassett et al. (2016)	3.8 - 4.5	4.5 - 7.9